Relaxation experiments with synchrotron radiation

O. Leupold [a,*] and H. Winkler [b]

[a] *II. Institut für Experimentalphysik, Universität Hamburg, D-22761 Hamburg, Germany*
[b] *Institut für Physik, Medizinische Universität zu Lübeck, D-23538 Lübeck, Germany*

Relaxation phenomena show up in standard energy-domain Mössbauer spectra via line broadening. The evaluation of such spectra is in most cases done by applying the stochastic theory of lineshape mainly developed in the 60's and 70's. Due to the time structure and the polarization of the synchrotron radiation nuclear resonance forward scattering in the time domain gives valuable additional information on relaxation mechanisms. We report here mainly on Nuclear Forward Scattering (NFS) experiments, investigating the paramagnetic relaxation of high-spin Fe^{2+} and Fe^{3+} ions, superparamagnetic relaxation and briefly on recent investigations of charge fluctuations in Eu_3S_4.

1. Introduction

Mössbauer spectroscopy is very sensitive to relaxation phenomena in solids if the relaxation times are comparable to the Larmor precession times of the nuclei. In this context relaxation means fluctuation between different states of a system, e.g., between the electronic states of one atom or between different orientations of the magnetization in small superparamagnetic particles. The evaluation of such spectra is in most cases done by adopting the stochastic theory mainly developed in the 60's and 70's by Blume and others [1,2] (for a review see [3, chapters 1, 11, 12]).

The stochastic models take advantage of the description of the hyperfine interaction in terms of *effective hyperfine fields* acting on the nuclei. These effective fields can either originate from the magnetization in small particles, which is the case in superparamagnetism, or from the electronic states of a paramagnetic ion. In the latter case the concept of effective hyperfine fields is a very good approximation if the energy splittings in the electron shell – either due to crystal fields, spin–orbit coupling or external magnetic fields – are large compared to the hyperfine interaction energies.

Generally, one can distinguish between three time regimes:

(a) If the relaxation time $\tau_R \gg 1/\omega_{hf}$ (*slow relaxation* limit, ω_{hf} is related to the hyperfine interaction energy E_{hf} via $E_{hf} = \hbar\omega_{hf}$), the nuclei experience the hyperfine field of each electronic state. This shows up in the spectrum like a superposition of various subspectra (with sharp resonance lines). The relative intensities of the subspectra are governed by the Boltzmann population of the electronic levels. The

* Present address: Nuclear Resonance Group, ESRF, B.P. 220, F-38043 Grenoble, France.

features of the corresponding Mössbauer spectrum are very similar to those of compounds with Mössbauer atoms on different sites in a crystal.
In a Nuclear Forward Scattering (NFS) experiment the hyperfine interactions manifest themselves as pronounced quantum beats which modulate the decay of the nuclear exciton.

(b) If $\tau_R \ll 1/\omega_{hf}$ (*fast relaxation* limit), the nucleus "sees" a hyperfine field, which is the weighted average (both in value and direction) of the individual fields of all electronic levels resulting in sharp resonance lines in the Mössbauer spectrum. Again, in NFS the "usual" quantum beats and dynamical beats are observed.

(c) Relaxation effects become visible in Mössbauer spectroscopy if the relaxation time τ_R is comparable to $1/\omega_{hf}$, and show up as line broadenings in the energy spectra. This is sometimes called the *intermediate relaxation* regime.

In the following we present NFS investigations of different systems, where relaxation phenomena have been observed also in conventional Mössbauer spectroscopy.

– Paramagnetic relaxation studied both in high-spin Fe^{2+} and Fe^{3+} systems, here $[Fe(CH_3COO)(TP_{piv}P)]^-$ and $(NH_4)Al_{0.95}{}^{57}Fe_{0.05}(SO_4)_2 \cdot 12H_2O$, respectively.
– Superparamagnetic relaxation on bacterioferritin from *Streptomyces olivaceus*.
– Charge fluctuations in Eu_3S_4.

A typical setup for NFS – here that at the wiggler beamline BW 4 at HASYLAB (DESY, Hamburg) – is shown in figure 1.

Two successive monochromators for the synchrotron radiation deliver an energy band width of ≈7 meV at 14.413 keV, the resonance energy of ^{57}Fe (for details cf. [4]). A liquid helium bath cryostat with two superconducting split pair magnets

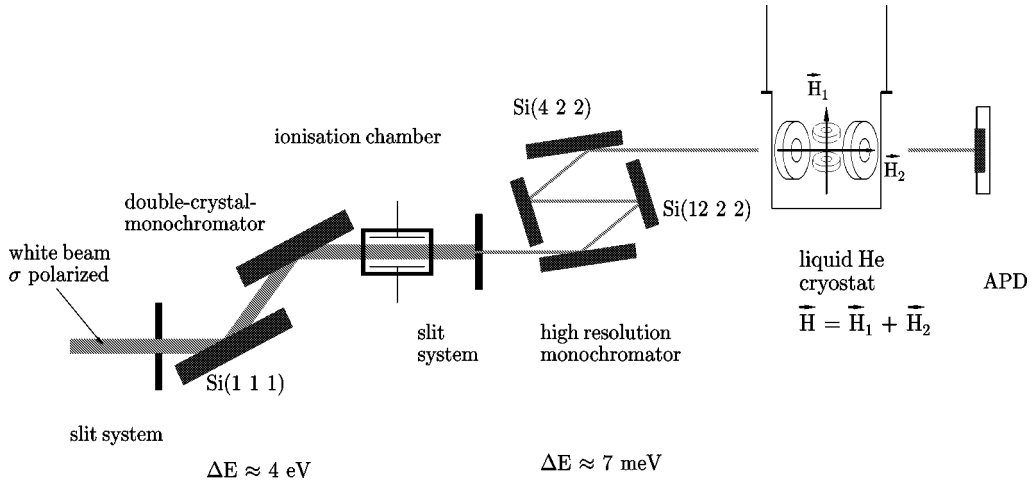

Figure 1. Experimental setup at BW 4 for nuclear forward scattering of synchrotron radiation at the 14.413 keV resonance of ^{57}Fe.

in orthogonal setting can be used for measurements in high magnetic fields and at variable temperature. As fast detector an avalanche photodiode (APD) with a time resolution of ≈1 ns [5] is used.

2. Paramagnetic relaxation

2.1. *High-spin Fe^{2+} in [Fe(CH_3COO)($TP_{piv}P$)]$^-$*

Paramagnetic relaxation can successfully be described in the framework of the stochastic theory of lineshape developed by Clauser and Blume [2]. In this theory the time evolution of the nuclear hyperfine states during the scattering process is determined by the Liouville operator [6]

$$\widehat{L} = \frac{1}{\hbar} H_n^{\times} + \mathrm{i}\widehat{W}. \tag{2.1}$$

Here $H_n^{\times}$ is a superoperator which is associated with the nuclear hyperfine Hamiltonians $H^{(g),(e)}$ in the slow relaxation limit; its matrix elements are

$$\langle f', i'; \ell' | H_n^{\times} | f, i; \ell \rangle = \big(\langle f'; \ell | H^{(e)} | f; \ell \rangle \delta_{ii'} - \langle i; \ell | H^{(g)} | i'; \ell \rangle \delta_{ff'} \big) \delta_{\ell\ell'}, \tag{2.2}$$

where f and i indicate the hyperfine substates of the excited and ground nuclear level and ℓ enumerates the so called "stochastic states" with energies ε_ℓ which according to the model are switched on at random in the course of time. $\widehat{W}$ is the relaxation matrix with elements $w_{\ell\ell'}\delta_{ii'}\delta_{ff'}$ where the $w_{\ell\ell'}$ are probabilities of the transition jumps $\ell' \to \ell$ with $\varepsilon_{\ell'} \leqslant \varepsilon_\ell$, which satisfy the detailed balance condition:

$$w_{\ell'\ell} = w_{\ell\ell'} \exp\big[(\varepsilon_\ell - \varepsilon_{\ell'})/k_{\mathrm{B}}T\big]. \tag{2.3}$$

The diagonal elements $w_{\ell\ell}$ are given by

$$w_{\ell\ell} = -\sum_{\ell'} w_{\ell'\ell}. \tag{2.4}$$

In such a stochastic model the resonant transition frequencies in the forward scattering amplitudes are determined by the operator $[(\omega - \omega_r - \mathrm{i}\Gamma_0/2\hbar)\widehat{E} - \widehat{L}]^{-1}$, where ω_r is the transition frequency in the case of zero hyperfine splitting, Γ_0 is the transition width determined by the inverse lifetime of the excited state of the nucleus and $\widehat{E}$ is the unit superoperator. After diagonalization of this operator the mean forward scattering amplitudes $\bar{f}_{\alpha\beta}(\omega)$ have the following form:

$$\bar{f}_{\alpha\beta}(\omega) = \frac{1}{8\pi^2}\frac{b}{d}\int_0^{\pi} \sin\theta \,\mathrm{d}\theta \int_0^{2\pi}\int_0^{2\pi} \mathrm{d}\varphi \,\mathrm{d}\psi \sum_{\ell} w_\ell \sum_{\mu\mu'=\pm1,0} (-1)^{\mu} \times \Pi_{\alpha-\mu}(\psi,\theta,\varphi)\Pi_{\beta\mu'}(\psi,\theta,\varphi) \sum_n \frac{\bar{A}^{(n)}_{\mu\mu'}(\theta,\varphi)}{(\omega_r - \omega + \bar{\omega}_n(\theta,\varphi) - \mathrm{i}\Gamma/2\hbar)}, \tag{2.5}$$

where d is the geometric thickness, $T_{\mathrm{M}} = 4b\hbar/\Gamma$ the effective thickness of the sample, ψ, θ, φ are the Euler angles which specify the orientations of the molecules with respect to the laboratory frame of reference and $\Pi_{\alpha\mu}(\psi,\theta,\varphi)$ are combinations of the Wigner functions $D^1_{\mu\mu'}(\psi,\theta,\varphi)$ [7,8] of the form:

$$\Pi_{x\mu} = \frac{1}{\sqrt{2}}\left(D^1_{1\mu} - D^1_{-1\mu}\right) \quad \text{and} \quad \Pi_{y\mu} = \frac{\mathrm{i}}{\sqrt{2}}\left(D^1_{1\mu} + D^1_{-1\mu}\right). \tag{2.6}$$

In eq. (2.5) the renormalized transition frequencies $\overline{\omega}_n(\theta,\varphi;\ell)$ are complex quantities:

$$\overline{\omega}_n(\theta,\varphi;\ell) = \Omega_n(\theta,\varphi;\ell) - \frac{\mathrm{i}}{2\hbar}\Gamma_n(\theta,\varphi;\ell), \tag{2.7}$$

where n enumerates the nuclear transitions in the molecules with the given orientation. The number of these transitions is the same as in the case of slow relaxation, $(2I_{\mathrm{g}} + 1)\cdot(2I_{\mathrm{e}} + 1)\cdot(2S + 1)$, where I_{e} and I_{g} are the values of the nuclear spin in the excited and ground states, respectively. But instead of simple relative weights of the transitions we have complex quantities $\bar{A}^{(n)}_{\mu\mu'}$, which result from the components of the corresponding eigenvectors.

When the relaxation transitions are uncorrelated in different molecules the response function of the system $\widetilde{R}_{\alpha\beta}(\omega)$ can be expressed in terms of the forward scattering amplitudes as described in [8]. The only difference here is that the forward scattering amplitudes (eq. (2.5)) are modified in a characteristic manner. The most significant result for paramagnetic relaxation with intermediate rate is the significant reduction of the quantum beat structure of the scattered radiation pulse. We note that in the slow relaxation limit the quantum beat structure arises due to narrow peaks in a broad nuclear absorption spectrum. As the probabilities of jumps $w_{\ell\ell'}$ increase, the corresponding changes of the scattering amplitudes $\bar{f}_{\alpha\beta}(\omega)$ (the increase of the additional widths of the transition lines Γ_n first of all) cause a smearing of such peaks. The result is that the scattered radiation decays fast in comparison with the nuclear lifetime $\tau_n = \hbar/\Gamma_0$ and that the oscillating structure is very smeared. When relaxation becomes faster ($w_{\ell\ell'} > |\omega_n|$) the situation changes again. Now most of the transitions become very broad and have very small relative weights. On the other hand, for the intensive transitions the $\Gamma_n(\theta,\phi)$ go to zero. The number of such transitions is $(2I_{\mathrm{e}}+1)\cdot(2I_{\mathrm{g}}+1)$ for each orientation of the paramagnetic molecules. Here the quantum-beat structure of the scattered radiation pulse appears again although a smaller number of transitions is associated with it. The conditions of the fast relaxation limit, described above, are fulfilled in this case and the corresponding formulae of paper [8] can be used in the calculations.

Note that the fast dying out of the pulses of coherently scattered radiation described above does not mean the switching off of the decay of the excitation produced by the primary synchrotron radiation pulse in the sample. Due to incoherent processes (such as incoherent or multiphonon scattering or electron conversion) this decay goes on until the sample has lost the stored energy (where the nuclear lifetime $\hbar/\Gamma_0$ is the characteristic relaxation time for the energy relaxation of the system).

But simultaneously, an intensive dephasing phenomenon may take place in the sample, caused, for example, by a substantial spread of the nuclear transition frequencies or by paramagnetic relaxation of intermediate rate. Then the phase memory of the system can be lost in a time interval much shorter than $\hbar/\Gamma_0$ (phase relaxation of the system). This means the decay of the coherent nuclear polarization as well as the decay of the strictly forward directed pulse of coherently scattered radiation, coupled to such polarization. The behavior of this forward scattered pulse of radiation has been studied in this paper as well as in [8]. The situation here is analogous to the paramagnetic resonance experiments where the stages of the transversal (loss of the phase memory) and the longitudinal (loss of the excess energy) relaxation can be distinguished in the relaxation process.

Paramagnetic systems of great importance for Mössbauer spectroscopy are, of course, iron containing molecules with unpaired spins which couple to a total spin S. Under the influence of ligand fields (zero-field interaction) and applied magnetic fields (Zeeman interaction) the $(2S+1)$-fold degeneracy of the paramagnetic state is lifted. In figure 2 the behavior of a ferrous high-spin complex with parameters taken from the iron porphyrin complex presented below is demonstrated. Paramagnetic relaxations, usually denoted after their mechanism spin–lattice or spin–spin relaxation, take place in the form of random transitions in time between these spin (sub-)states which we can identify with the stochastic states of the model.

The magnetic hyperfine field is different for the $2S+1$ spin states with respect to its magnitude and direction. Consequently, the absorption pattern of a particular nucleus depends on the electronic spin states occupied at a certain temperature. The more spin states are thermally populated the larger is the number of resonances which

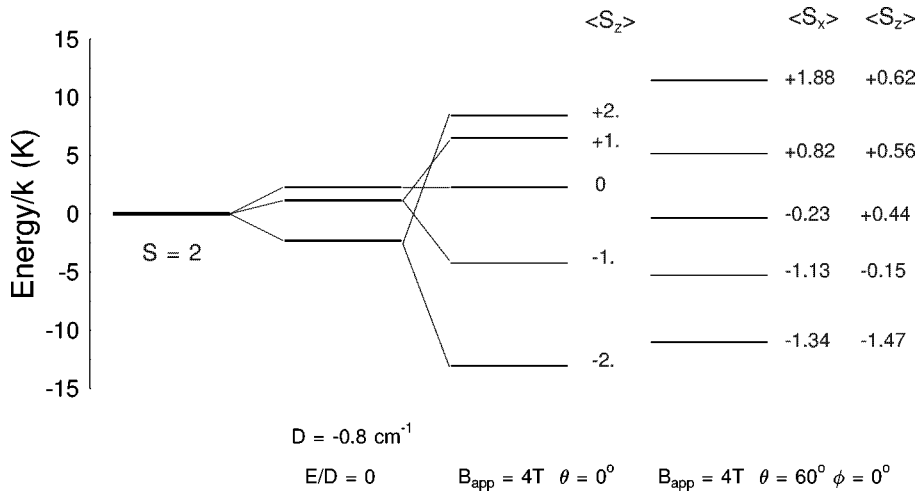

Figure 2. Splitting of the spin state of a ferrous high-spin complex under the influence of the zero-field splitting and Zeeman interaction. $\langle S_x \rangle$ and $\langle S_z \rangle$ are the spin expectation values in the corresponding magnetic substates.

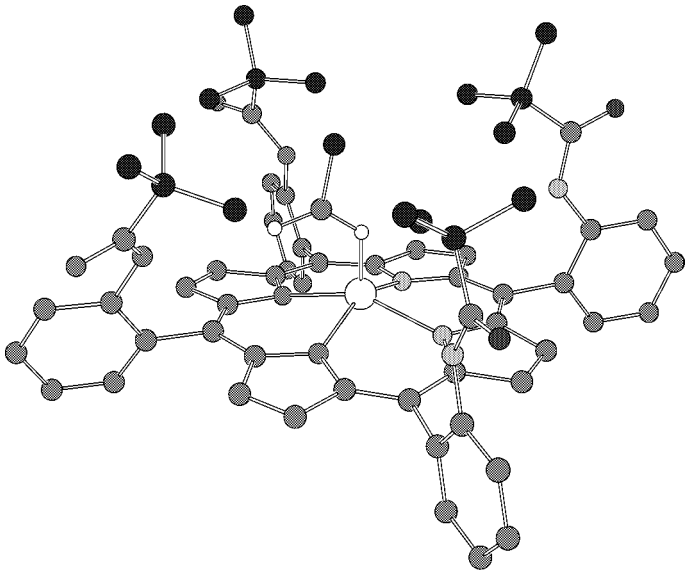

Figure 3. The "picket-fence" iron porphyrin complex $[Fe(CH_3COO)(TP_{piv}P)]^-$.

are accessible to the incoming beam. When, however, phonons of the appropriate energy are available, transitions between the various spin states are induced. At low temperatures (for high-spin ferrous complexes often up to about 30 K) the rate is expected to be of the same order of magnitude as the Larmor frequencies and a pattern which arises from the so-called intermediate relaxation will be observed. At higher temperatures the spin states become more and more equally populated and the transition rates get much faster than the hyperfine frequencies, so that the magnetic hyperfine interaction is reduced to zero and only the electric quadrupole interaction, which is practically independent of the spin states, remains.

The so-called "picket-fence" iron porphyrin complex $[Fe(CH_3COO)(TP_{piv}P)]^-$ (figure 3) has been extensively studied by us with respect to its paramagnetic properties because it forms to some extent a model complex for the cytochrome P460 of the multi-heme enzyme hydroxylamine oxido-reductase [9]. It is a high-spin ferrous complex and its spin-Hamiltonian parameters are, after readjustment to the recent measurements $D = -0.8$ cm^{-1} with $E/D = 0$ for the zero-field splitting, $A_{x,y}/g_n\beta_n = -16.5$ T and $A_z/g_n\beta_n = -12.0$ T for the magnetic hyperfine coupling parameters and $\Delta E_Q = 4.25$ mm/s with $\eta = 0$ for the quadrupole splitting. Figure 4 shows the conventional Mössbauer spectra obtained at various temperatures in a field of 4 T applied perpendicularly to the γ-ray. Figure 5 gives the corresponding time-dependent NFS spectra taken with the setup available at beam line BW4 of HASYLAB in Hamburg (cf. figure 1) from a sample of effective thickness $t_{\text{eff}} \approx 20$. The external field again had a strength of 4 T and was applied perpendicularly to the wave vector $\vec{k}_\gamma$ and to the polarization (electric field vector) $\vec{e}_\sigma$ of the incoming beam.

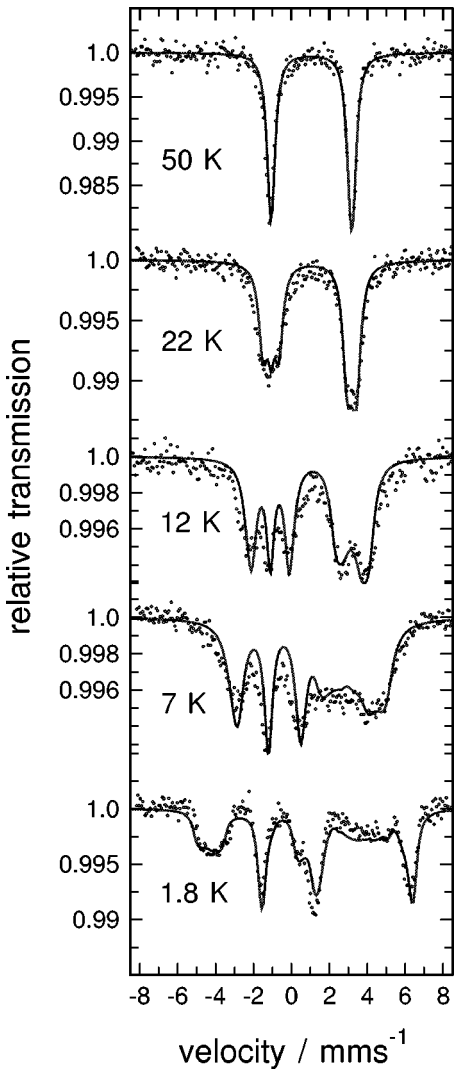

Figure 4. Conventional Mössbauer spectra of complex $[Fe(CH_3COO)(TP_{piv}P)]^-$ taken at the temperatures indicated and in a field of 4 T applied perpendicularly to the γ-ray.

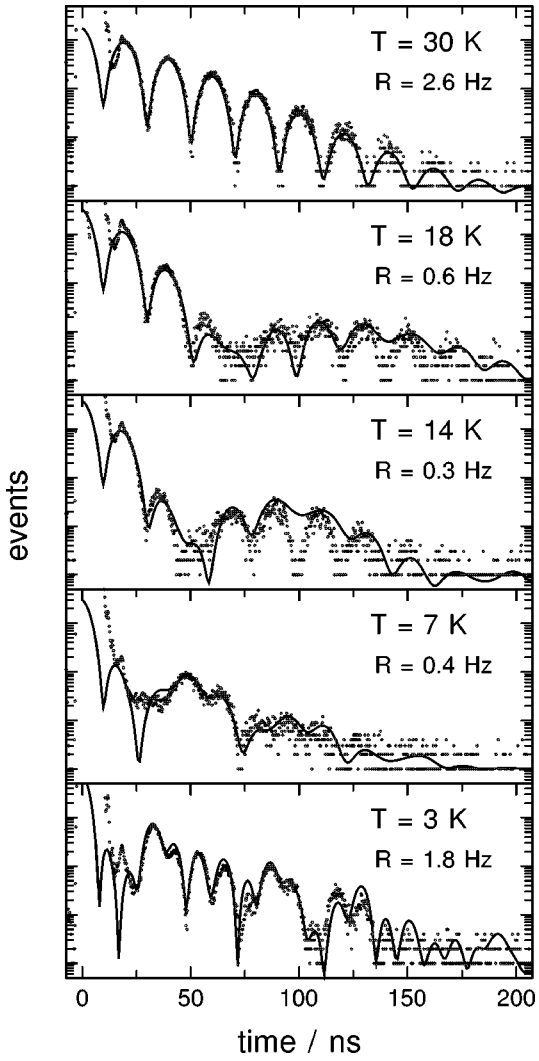

Figure 5. Time dependence of the nuclear resonant forward scattering (NFS) by the complex $[Fe(CH_3COO)(TP_{piv}P)]^-$ measured at the temperatures indicated and in a field of 4 T applied perpendicularly to the γ-ray and to the plane of the synchrotron. R denotes the integral rate of delayed counts between 25 and 250 ns observed during the data acquisition.

To calculate the forward scattered synchrotron radiation pulses the program SYNFOS of [8] has been modified appropriately by replacing the original expression for the forward scattering amplitudes by that of eq. (2.5). The case of the interaction of the electronic spin with the acoustic phonons of long wavelength has been considered in

the Debye continuum model. Here the one-phonon transition probabilities have been expressed as follows:

$$w_{\ell\ell'} = w_0 \cdot \frac{[|\varepsilon_\ell - \varepsilon_{\ell'}|/k_\mathrm{B}]^p}{\exp\left[|\varepsilon_\ell - \varepsilon_{\ell'}|/k_\mathrm{B}T\right] - 1}. \tag{2.8}$$

Two additional fitting parameters appear in eq. (2.8):

1. The constant w_0, which determines the strength of spin–phonon coupling. It depends on the electronic transition matrix elements, phonon frequency distribution parameters etc., but its dependence on the spin substate indices ℓ, ℓ' as well as on the temperature of the sample have been neglected in our approximation.

2. The power-index p which is 3 in the Debye approximation. By varying it, we may compensate to some extent the imperfection of the coarse continuum model.

Taking $p = 3$, one single value of $3.65 \cdot 10^5$ rad s^{-1} K^{-3} for the scaling parameter w_0 turns out to be appropriate to reproduce the spectra in both series at all measured temperatures. When performing, however, the angular integration required for the powder samples used in the measurement, it turned out that a certain degree of texture has to be taken into account. This has been done in a consistent manner in all fits.

The effect of dephasing can be read from the values of R in figure 5. They give the integral rates of delayed counts between 25 and 250 ns as observed in the experiment. These values obviously go through a minimum at 14 K. In figure 6 the temperature dependence of the experimental R is compared with the values obtained from the theoretical curves when the corresponding time integration is performed and

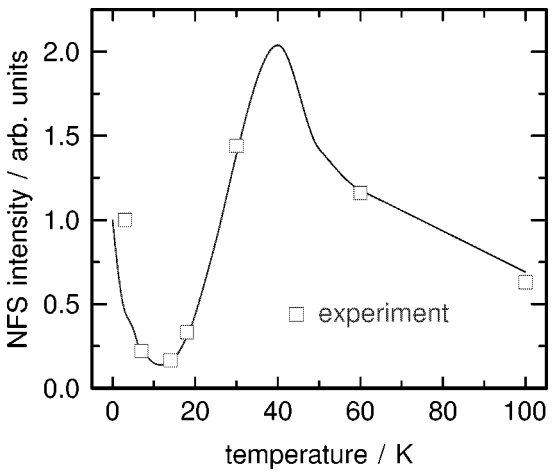

Figure 6. The temperature dependence of the experimental R compared with the values which are obtained from the theoretical curves. The corresponding time integration is performed between 25 and 250 ns and the results are normalized to unity at 0 K or at the lowest experimentally achieved temperature, respectively.

the results are normalized to unity at 0 K or at the lowest experimentally achieved temperature, respectively.

2.2. High-spin Fe^{3+} in $(NH_4)Al_{0.95}{}^{57}Fe_{0.05}(SO_4)_2 \cdot 12H_2O$

The approximation of effective hyperfine fields acting on the nuclei can be applied in the case of $(NH_4)Al_{0.95}{}^{57}Fe_{0.05}(SO_4)_2 \cdot 12H_2O$ in sufficiently strong external magnetic fields [11], where the spin–lattice relaxation of the Fe^{3+} impurity ion in $(NH_4)Al(SO_4)_2 \cdot 12H_2O$ was extensively treated. So this system was chosen as a model compound for the investigation of temperature dependent relaxation phenomena on a high spin Fe^{3+} system by nuclear resonance scattering in the time domain [12]. The stochastic theory of the line shape in energy domain Mössbauer spectroscopy developed by Blume [1] (for a review see [3, chapters 1, 11, 12]) was included in the CONUSS program package [10] by Sturhahn. The numerical treatment of the "relaxation part" involves the same superoperator formalism [1,2] as the Fe^{2+} case described above. The ^6S electronic ground state of the Fe^{3+}-ion requires, however, a different theoretical model for the relaxation rates in between the Zeeman split electronic states, which will be given in some detail below.

2.2.1. Experimental

Several single crystalline samples of $(NH_4)Al_{0.95}{}^{57}Fe_{0.05}(SO_4)_2 \cdot 12H_2O$ and $(NH_4)Fe(SO_4)_2 \cdot 12H_2O$ were prepared in the group of de Waard at the University of Groningen. Nuclear forward scattering experiments were performed at the wiggler beam line BW 4 at HASYLAB (DESY, Hamburg). The storage ring was operated in 2-bunch and 5-bunch mode yielding bunch distances of 480 ns and 192 ns, respectively. The setup for NFS is shown in figure 1. The samples were measured at temperatures between 3.5 and 250 K in a liquid helium bath cryostat supplied with two superconducting split pair magnets in orthogonal setting. In most cases an external field of 2 T was applied either in the vertical direction, i.e., perpendicular both to the beam and the polarization of the incident beam (in the following denoted as σ polarization) or parallel to the beam. In the first mentioned field geometry the "simplest" quantum beat pattern is expected, since only the $\Delta m = 0$ transitions are excited.

The measured time spectra of $(NH_4)Al_{0.95}{}^{57}Fe_{0.05}(SO_4)_2 \cdot 12H_2O$ as a function of temperature are shown in figure 7. The spectra at temperatures below 30 K were fitted under the assumption of slow relaxation between the electronic states. The fitted curves are shown as solid lines. Spectra measured at higher temperatures cannot be interpreted with static hyperfine interactions. The solid curves shown for temperatures $T \geqslant 150$ K are simulations adopting the stochastic relaxation model described below. However, the temperature range of the cryostat was not sufficient to reach the fast relaxation regime, where again sharp resonance lines should appear resulting from one static hyperfine field. In this limit the energy and time spectra are mainly determined by the external magnetic field, since the average of the internal fields tends to zero, when all Zeeman states are equally populated at high temperatures.

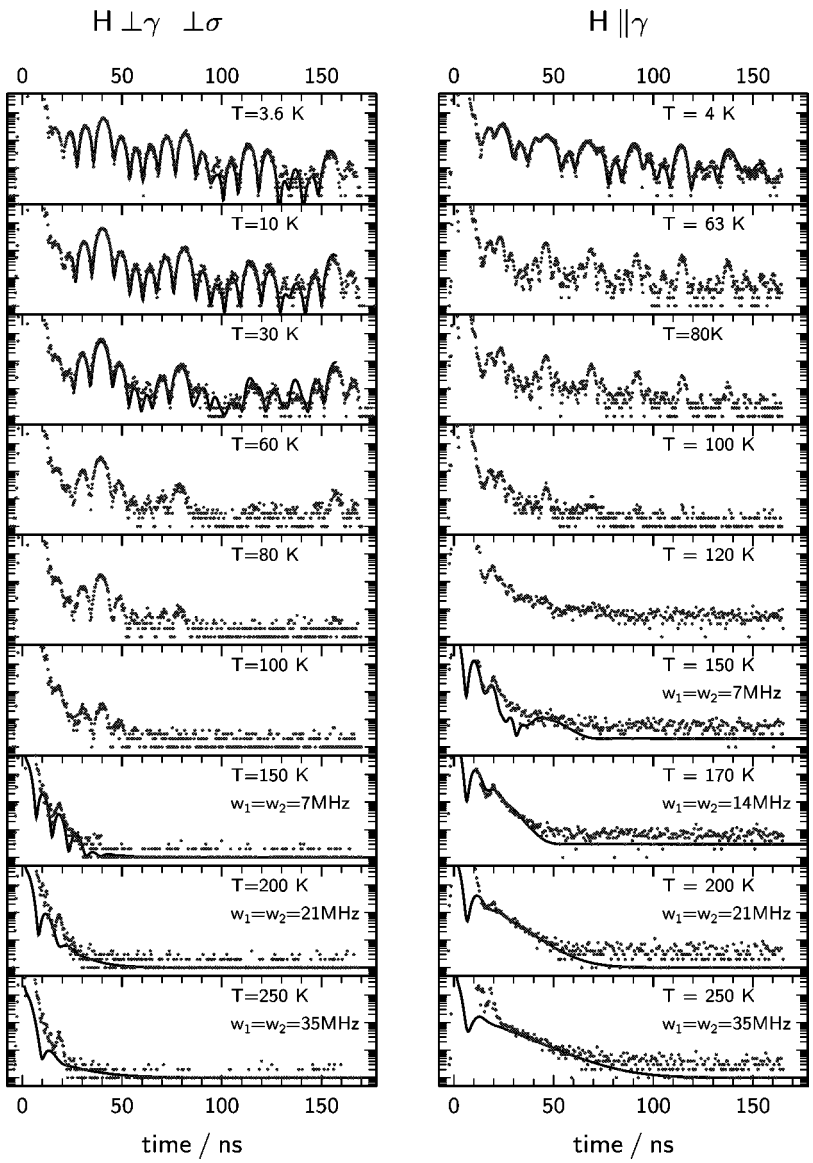

Figure 7. Time spectra of $(NH_4)Al_{0.95}{}^{57}Fe_{0.05}(SO_4)_2 \cdot 12H_2O$ measured in an applied field of 2 T and at different temperatures as indicated in the figure. The solid lines in the spectra at low temperatures are fits adopting the dynamical theory on nuclear resonant scattering [10] under the assumption of slow relaxation between the electronic states. At high temperatures the solid lines reveal simulations adopting the relaxation model described in the text with values for w_1 and w_2 as indicated in the figure.

The ratio of nonresonant (prompt) to resonant (delayed) quanta is about $5 \cdot 10^5$. This makes electronic suppression of the high prompt count rate necessary in order not to overload the detector electronics. Electronic artefacts like the “peak” at ≈20 ns observable at high temperatures and false side bunches spoil some time spectra at times

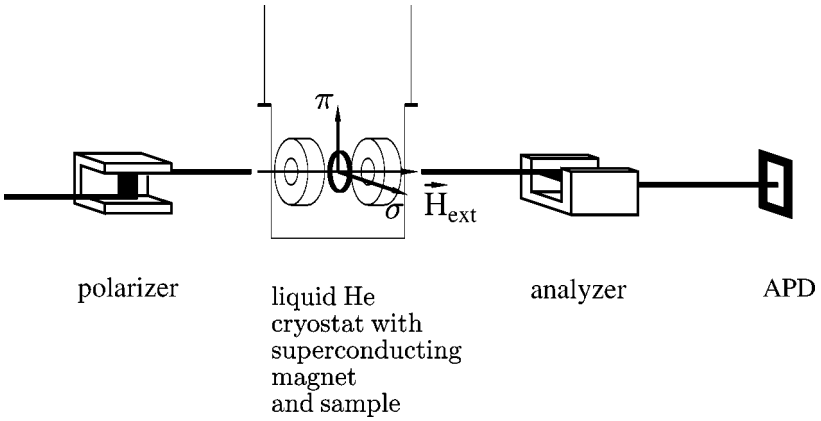

Figure 8. Experimental setup at APS for nuclear forward scattering of synchrotron radiation adopting the crossed polarizer/analyzer technique.

close to zero, just in the region expected to be most sensitive to relaxation effects. That is why it appeared necessary to reduce the ratio of nonresonant to resonant intensity. One possibility is to apply crossed polarizers.

In figure 8 we show the setup at APS (beamline 3 ID [13]) utilizing the crossed polarizer/analyzer technique (cf. [14]). The storage ring was operated in a special timing mode with 30 bunches having a bunch distance of 102 ns and an additional $\approx$600 ns time gap. The radiation hitting the sample is σ-polarized to more than 99.9% after the first (polarizer) channel cut crystal. The prompt radiation is suppressed to $\sim 10^{-7}$ [14] after the second (analyzer) crystal, that predominantly transmits π-polarized radiation. But, if in the nuclear scattering process the polarization is changed from pure σ to a tiny admixture of π, the delayed (resonant) radiation can pass the analyzer and is detected by the APD detector. This polarization rotation ("γ-optical activity") by the sample can be achieved by applying a sufficiently strong external magnetic field at the sample in an appropriate direction. In the case presented here H_{ext} was parallel to the direction of the γ-ray.

Due to the almost total suppression of the prompt intensity it is possible to observe nuclear scattered delayed quanta much earlier (almost from $t = 0$ on) than in the "standard" NFS setup. The forward scattered intensity from $(NH_4)Al_{0.95}{}^{57}Fe_{0.05}(SO_4)_2 \cdot 12H_2O$ at different temperatures (figure 9) clearly shows this advantage of the polarizer/analyzer setup. Additionally, there are structures observable in the high temperature time spectra at about 50 ns which were not present in the NFS spectra taken at BW 4.

2.2.2. The Fe^{3+} ion – electronic states and relaxation

The electron configuration of a free Fe^{3+} ion is shown in figure 10(a). It consists of the full Ar shells and a half filled $3d$ shell. The resultant ground state is a $^6S_{5/2}$ state, i.e., total orbital momentum $L = 0$, total spin $S = 5/2$. In a crystal the degeneracy of the ground state can be lifted by the crystal field and/or an external magnetic field

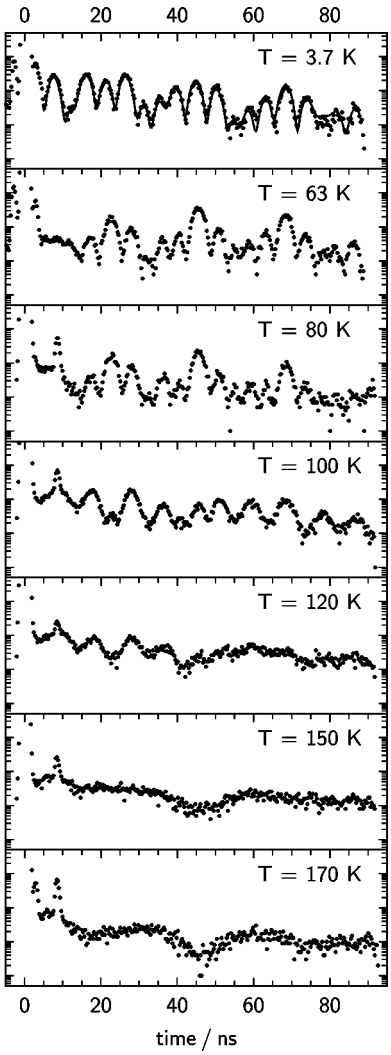

Figure 9. Time spectra of $(NH_4)Al_{0.95}{}^{57}Fe_{0.05}(SO_4)_2 \cdot 12H_2O$ measured with the crossed polarizer setup in an applied field of 2 T parallel to the beam and at different temperatures as indicated in the figure. At $T = 3.7$ K the spectrum can be fitted assuming the slow relaxation limit (solid line).

acting on the ion. The total Hamiltonian of the Fe^{3+}-ion – neglecting the influence of the hyperfine interaction on the electronic states – can be written as

$$\widehat{H}_{\text{tot}} = \widehat{H}_{\text{cf}}^{(0)} + \widehat{H}_Z, \tag{2.9}$$

where the static crystal field Hamiltonian $\widehat{H}_{\text{cf}}^{(0)}$ is usually written in terms of the spin-Hamiltonian formalism as

$$\widehat{H}_{\text{cf}}^{(0)} = D \cdot \left[\widehat{S}_z^2 - \frac{1}{3}S(S+1)\right] + E \cdot \left(\widehat{S}_x^2 - \widehat{S}_y^2\right). \tag{2.10}$$

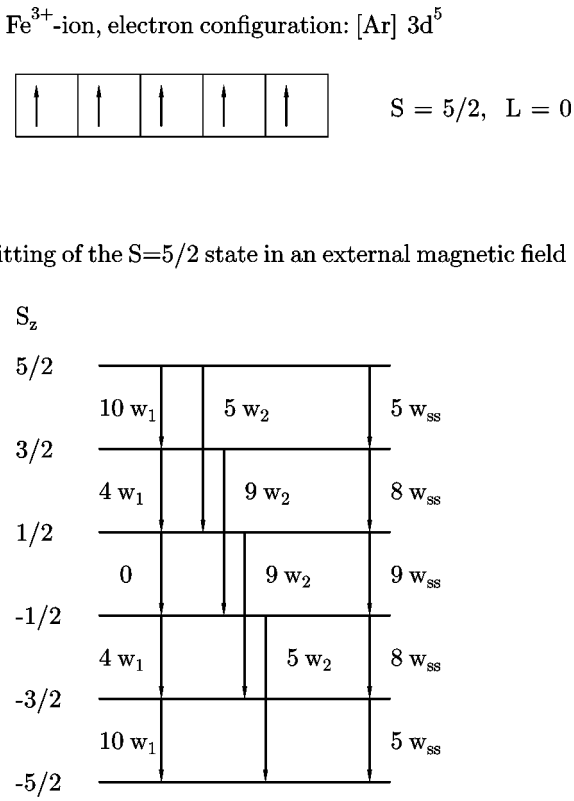

Figure 10. (a) Electron configuration of a free Fe^{3+} ion. (b) Splitting of the $S = 5/2$ ground state in an external magnetic field and the possible transitions between different substates due to spin–lattice relaxation (parameters w_1 and w_2) and spin–spin relaxation (parameter w_{ss}).

In the case of an axially symmetric crystal field the so called rhombicity parameter vanishes, i.e., $E = 0$. Higher order terms can be neglected for $(NH_4)Al_{0.95}{}^{57}Fe_{0.05}(SO_4)_2 \cdot 12H_2O$ [11].

For fields larger than ≈2 T the Zeeman interaction

$$\widehat{H}_Z = 2\mu_B \vec{B} \cdot \vec{S} \tag{2.11}$$

exceeds the crystal field interaction in $(NH_4)Al_{0.95}{}^{57}Fe_{0.05}(SO_4)_2 \cdot 12H_2O$ by more than one order of magnitude [11]. Thus the Zeeman sublevels are to good approximation almost pure S_z eigenstates, even if the quantization axis of the crystal field operator is not collinear with the external magnetic field. The resultant energy levels of the $S = 5/2$ ground state are shown in figure 10(b), where pure Zeeman interaction was assumed. In an external field of 2 T the total energy splitting $\varepsilon(S_z = 5/2) - \varepsilon(S_z = -5/2)$ is about 1 meV.

The effective hyperfine field approximation is used in order to calculate the spectra shown below. The effective hyperfine field of each m_S sublevel is given by

$$B_{\text{eff}}(m_S) = B_{\text{ext}} + B_{\text{C}} m_S \tag{2.12}$$

and is either parallel or antiparallel to the external field. The only free parameter, B_{C}, is a Fermi contact term arising from the polarization of the s-electrons due to exchange interaction with the 3d electrons (cf. [3, chapter 1]). The treatment of the relaxation problem requires the solution of the superoperator Hamiltonian yielding a total number of $(2I_{\text{g}} + 1) \cdot (2I_{\text{e}} + 1) \cdot (2S + 1) = 48$ transitions in the case of Fe^{3+}, where six electronic states have to be taken into account. The spin–lattice relaxation rates for a ^{6}S state were first calculated by Blume and Orbach [15] for the Mn^{2+}-ion in a cubic environment. Bhargava et al. [11] give an extensive outline of the relaxation processes important for the Fe^{3+}-ion. In the following we will briefly sketch their treatment.

The static crystal field Hamiltonian (eq. (2.10)), which represents the equilibrium position of the ligands, is extended by two terms, $\widehat{H}_{\text{cf}}^{(1)}$ and $\widehat{H}_{\text{cf}}^{(2)}$, which depend linearly ($i = 1$) and quadratically ($i = 2$), respectively, on the ligand displacements and reveal the dynamic part of the crystal field:

$$\begin{aligned}\widehat{H}_{\text{cf}}^{(i)} = {} & d^{(i)}\big[\widehat{S}_z^2 - \frac{1}{3}S(S+1)\big] + e^{(i)}\big(\widehat{S}_x^2 - \widehat{S}_y^2\big) + f^{(i)}\big(\widehat{S}_x\widehat{S}_y + \widehat{S}_y\widehat{S}_x\big) \\ & + g^{(i)}\big(\widehat{S}_x\widehat{S}_z + \widehat{S}_z\widehat{S}_x\big) + h^{(i)}\big(\widehat{S}_y\widehat{S}_z + \widehat{S}_z\widehat{S}_y\big).\end{aligned} \tag{2.13}$$

The operators $d,\ e,\ f,\ g,\ h$ act on the phonon states, whereas the $\widehat{S}_x,\ \widehat{S}_y,\ \widehat{S}_z$ act on the m_S substates of the $S = 5/2$ electronic ground state. As in the static Hamiltonian, only spin terms up to second order are taken into account. The relevant transitions between the m_S substates and their relative strengths are then given in units of two spin–lattice relaxation parameters, w_1 and w_2. Both the direct process and the Raman process contribute to each of these two parameters:

$$w_1 = \frac{4\pi}{\hbar}\sum_q \big\langle \big|\langle n_q + 1|g^{(1)} + \mathrm{i}h^{(1)}|n_q\rangle\big|^2\big\rangle_T \delta(\hbar\omega_q - \Delta_1), \tag{2.14}$$

$$w_2 = \frac{4\pi}{\hbar}\sum_q \big\langle \big|\langle n_q + 1|e^{(1)} + \mathrm{i}f^{(1)}|n_q\rangle\big|^2\big\rangle_T \delta(\hbar\omega_q - \Delta_2) \tag{2.15}$$

for one phonon contributions (direct process), and

$$w_1 = \frac{4\pi}{\hbar}\sum_{q,p} \big\langle \big|\langle n_q - 1, n_p + 1|g^{(2)} + \mathrm{i}h^{(2)}|n_q, n_p\rangle\big|^2\big\rangle_T \delta(\hbar\omega_q - \hbar\omega_p - \Delta_1), \tag{2.16}$$

$$w_2 = \frac{4\pi}{\hbar}\sum_{q,p} \big\langle \big|\langle n_q - 1, n_p + 1|e^{(2)} + \mathrm{i}f^{(2)}|n_q, n_p\rangle\big|^2\big\rangle_T \delta(\hbar\omega_q - \hbar\omega_p - \Delta_2) \tag{2.17}$$

for two phonon contributions (first order Raman process). Here $|n_p\rangle,\ |n_q\rangle$ are phonon states, $\omega_p,\ \omega_q$ the corresponding phonon frequencies and $\Delta_i,\ i = 1, 2$, the energy

differences between the electronic states involved in the fluctuation process. The transition frequencies w_1 and w_2 are evaluated in the frame of this model for a pure cubic environment, where in sufficiently strong external magnetic fields the electronic states are S_z eigenstates and the energy splitting between adjacent m_S states is constant for all states. In the system presented here the symmetry is lower than cubic, and is taken into account by the comparatively small axial crystal field parameter D, which results in slightly modified Boltzmann populations of the electronic states compared with the pure Zeeman interaction. The states remain S_z eigenstates since the Zeeman interaction is much stronger than the crystal field interaction. The influence of the lower symmetry on the rate parameters w_1 and w_2 is not taken into account.

All relevant transitions are shown in figure 10(b). The corresponding transitions for spin–spin relaxation governed by the parameter w_{ss} are also displayed in figure 10(b). Transition probabilities are always given for "downward" transitions. The probabilities for the corresponding "upward" transitions are – in thermal equilibrium – calculated in order to fulfill the principle of detailed balance given by eq. (2.3). Spin–spin relaxation is supposed to be less important in the case of the highly diluted ^{57}Fe in $(NH_4)Al_{0.95}{}^{57}Fe_{0.05}(SO_4)_2 \cdot 12H_2O$. The Mössbauer spectra presented in [11] and those measured by us in different longitudinal external magnetic fields up to 4 T at low temperatures (not shown) give no indication of intermediate relaxation. The moderate line broadenings of $\approx$0.2 mm/s are mainly due to the large effective thickness $t_{\text{eff}} \approx 30$ of our sample.

2.2.3. Results

All simulations and evaluations of time spectra were performed by adopting the program package CONUSS [10], where the stochastic relaxation theory following [1] was included. The time spectra of $(NH_4)Al_{0.95}{}^{57}Fe_{0.05}(SO_4)_2 \cdot 12H_2O$ taken at about 4 K under different conditions were evaluated assuming the slow relaxation limit. The spectra together with the fits are displayed in figure 11.

There were only three free parameters for fitting the four low temperature spectra, i.e.,

$$B_{\text{C}} = (23.44 \pm 0.10)\ \text{T}, \qquad t_{\text{eff}} = 29 \pm 3, \qquad D = (-0.15 \pm 0.05)\ \text{cm}^{-1}.$$

The absolute value obtained for the spin-Hamiltonian parameter D is significantly larger than that reported in the literature, $D = -0.025$ cm^{-1} [11]. D influences the relative populations of the lowest lying Zeeman substates of the ^{6}S ground state. A larger value of $|D|$ results in a relatively higher population of the $m_S = -5/2$ ground state. A significantly lower sample temperature would yield the same effect. These populations in turn govern the appearance of the "envelope" of the time spectrum. Since the same result for D was obtained from measurements performed in different cryostats, an error in the temperature calibration of the setup is very unlikely. The quadrupole splitting was found to be $eQV_{zz}/2 = 0$ within the fit error and was kept fixed at zero.

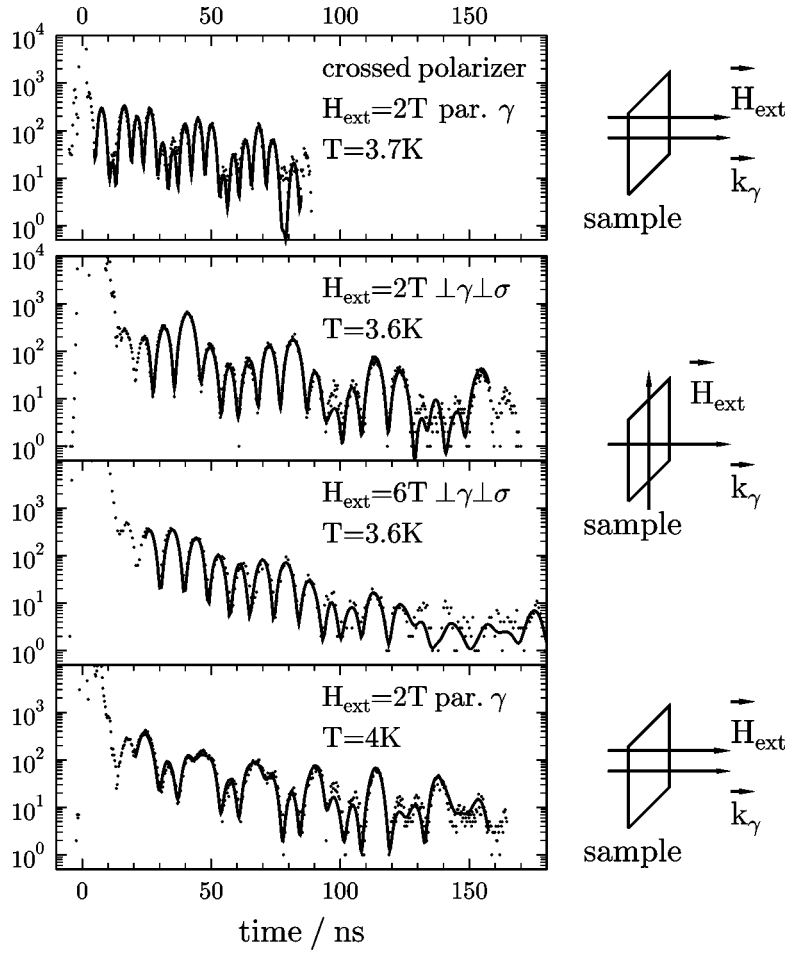

Figure 11. Time spectra of $(NH_4)Al_{0.95}{}^{57}Fe_{0.05}(SO_4)_2 \cdot 12H_2O$ measured at low temperatures under different experimental conditions as shown in the figure. The solid lines are fits adopting the dynamical theory on nuclear resonant scattering [10]. With crossed polarizer/analyzer (top) the fit is possible from 5 ns on, in the other cases from ≈20 ns on.

The spectra at higher temperatures can no longer be evaluated with the assumption of static hyperfine fields. Simulations were performed under the condition of fluctuating hyperfine fields in order to investigate the influence of the spin–lattice parameters w_1 and w_2 under different experimental conditions (cf. figure 7). At temperatures above ≈80 K the six Zeeman levels are approximately equally populated. Therefore, as a simplification, the same values were chosen for the relaxation rates "up" and "down" between each two electronic states. Spin–spin interaction is not taken into account.

The temperature dependence of w_1 and a value for the ratio w_1/w_2 obtained from Mössbauer spectroscopy are given in the literature [11], where – with a rather large uncertainty – a ratio of $w_1/w_2 = 2:1$ was found to give the best fits. To our present

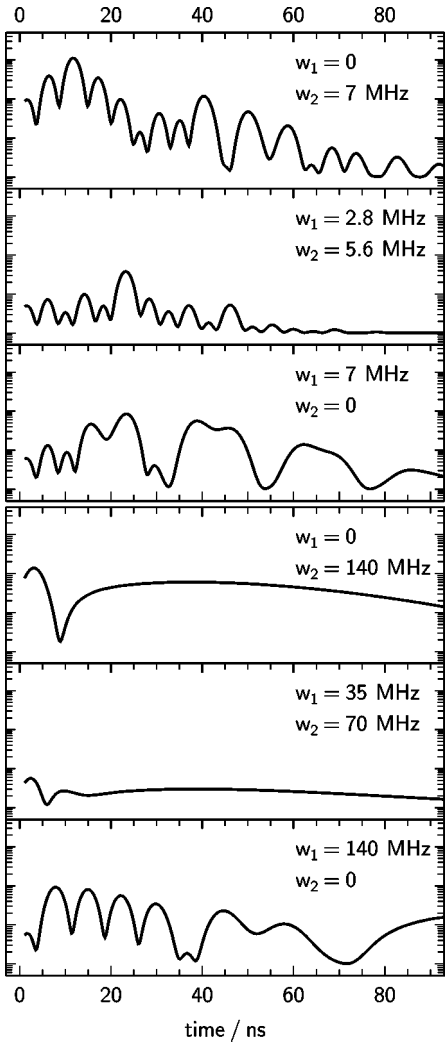

Figure 12. Simulations of time spectra of $(NH_4)Al_{0.95}{}^{57}Fe_{0.05}(SO_4)_2 \cdot 12H_2O$ assuming intermediate relaxation and equal population of the electronic states. Simulations at $H_{\text{ext}} \| \vec{k}_\gamma$ including polarizer/analyzer setup are shown for different values of w_1 and w_2 as indicated in the figure.

knowledge the data presented here do not yield a more accurate result for this ratio, since the simulations of the high temperature spectra do not have fit quality, yet. So $w_1 = w_2$ was chosen, which reproduces the shape of the high temperature time spectra reasonably.

Although the spectra taken in the crossed polarizer/analyzer geometry seem to exhibit more pronounced structures at elevated temperatures, the interpretation is not unique. The simulations shown in figure 12 are made for two regimes of values for the relaxation rates and different ratios of w_1/w_2. They should be compared with the measurements of figure 9 at temperatures above $\approx$100 K. At least qualitatively some

structures in the time spectra of the measured data can be reproduced, when assuming $w_2 = 0$. Other combinations of w_1 and w_2 give significantly worse results, especially – at the higher relaxation rates – no intensity minima in the time region between 30 ns and 70 ns. This effect will be the subject of further study.

3. Superparamagnetic relaxation

Superparamagnetism is a well-known phenomenon in magnetic single-domain particles. It is in practice often used to estimate the size of such particles and their degree of crystallinity. The model of collective magnetic excitations, which has been suggested years ago by Mørup and Topsøe (figure 13) [16] has proven to be appropriate in many cases for the interpretation of Mössbauer spectra taken from superparamagnetic samples. If the magnetic energy surface of a particle is given as shown in the figure, one expects that the magnetization fluctuates around its easiest direction.

If these fluctuations are fast, only the thermal average $M_S\langle\cos\theta\rangle_\mathrm{T}$ will have an effect and determine the magnetic hyperfine field. Thus in first approximation the hyperfine field decreases linearly with temperature. Now and again the system may cross the barrier and the magnetization flips by 180°. So we have superparamagnetism and a simultaneous shrinking of the magnetic hyperfine splitting. Mössbauer spectroscopy has introduced the concept of the blocking temperature for the characterization of superparamagnetic particles. By definition the temperature where the areas under the nonmagnetic quadrupole doublet and the magnetic sextet of a Mössbauer absorption spectrum are equal is called the blocking temperature because on the time scale of the Mössbauer spectroscopy the flipping of the magnetization begins to be blocked.

A biological system for which the particle size and crystallinity are properties of high interest is ferritin. Ferritins are storage proteins found in animals. They consist of

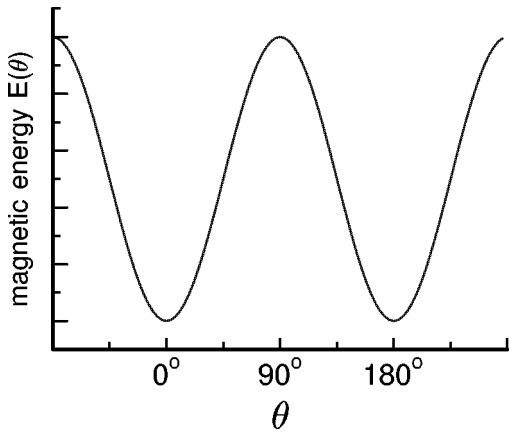

Figure 13. Magnetic energy as a function of the polar angle θ between the magnetization M_S of a superparamagnetic particle and an easy direction of magnetization for a magnetic single-domain particle with uniaxial anisotropy.

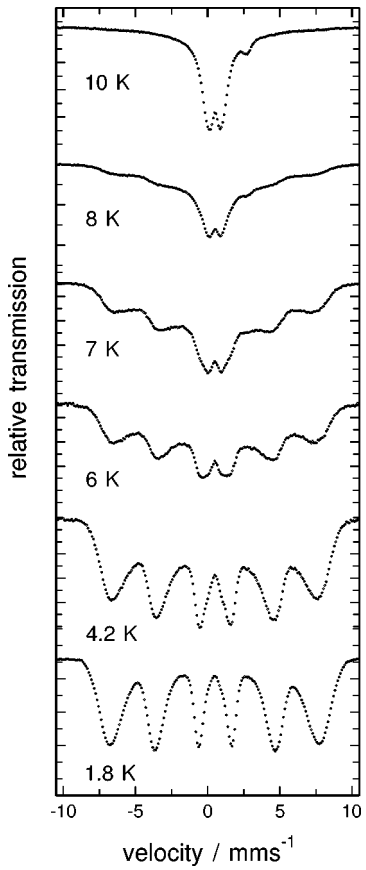

Figure 14. Mössbauer absorption spectra of the bacterioferritin from *S. olivaceus* measured at the temperatures indicated.

a protein shell and a mineral core containing essentially hydrated ferric oxide. These are in physical terms magnetic single-domain particles that exhibit a blocking temperature of around 40 K. In bacteria one finds bacterioferritin which is slightly different in that the core consists rather of hydrated phosphate. The observed blocking temperature is much lower, in the present system, coming from *Streptomyces olivaceus*, around 8 K. The conventional Mössbauer spectra (figure 14) [17] show the typical collapse of the magnetic sextet into a quadrupole doublet as a function of temperature.

However, the line broadenings at low temperatures and the triangular shape of the spectra around 8 K cannot be explained by a simple spin-flip model as worked out, e.g., by Wickman [18]. One has to take into account that a distribution of particle sizes and probably a variation in the degree of crystalline order is present in the sample, which would be accompanied by a distribution of hyperfine fields and of relaxation rates. The NFS shows fast beating below 8 K and slow beating from an electric quadrupole interaction at and above 10 K (figure 15(a)).

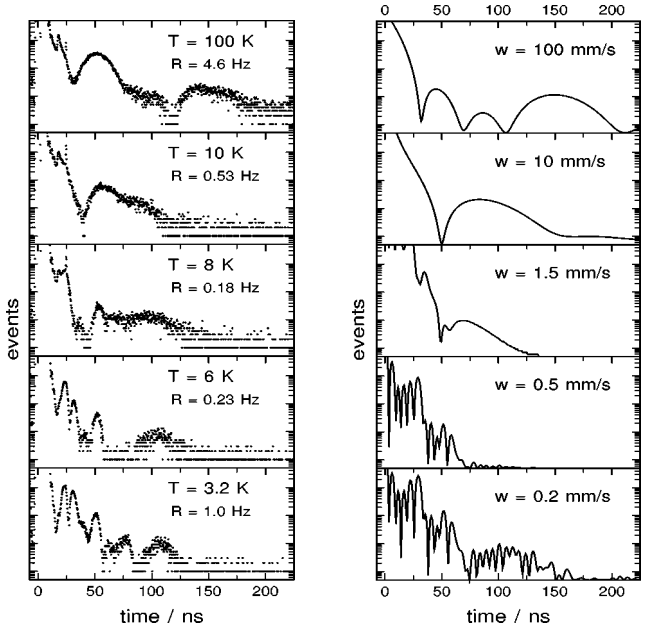

Figure 15. (a) Time-dependence of the nuclear resonant forward scattering (NFS) by the bacterioferritin from *S. olivaceus* measured at the temperatures indicated. R denotes the integral rate of counts delayed by more than 25 ns observed during the data acquisition. (b) Theoretical spectra calculated with SYNFOS taking for the hyperfine field $B_{\mathrm{hf}} = 45$ T, for the quadrupole splitting $\Delta E_{\mathrm{Q}} = 0.86$ mm/s, for the effective thickness $t_{\mathrm{eff}} = 60$ and for the jump rate w the values indicated (1 mm/s $\Leftrightarrow$ 73 MHz).

The general temperature behavior can be reproduced by theoretical calculations using the program package SYNFOS [19] as shown in figure 15(b), where, however, distributions have been neglected.

4. Charge fluctuations in Eu_3S_4

The ^{151}Eu resonance was only recently detected by NFS with synchrotron radiation [20]. Besides the interesting magnetic properties of Eu^{2+} compounds there are a large number of systems where mixed valencies and charge fluctuations occur (for a review on results obtained by conventional Mössbauer spectroscopy see, e.g., [21]). One example for charge fluctuations is Eu_3S_4, where it is known from Mössbauer spectroscopy that the temperature dependent fluctuation rates between the two valence states excellently fit to the experimentally accessible time window [22,23]. The experiments were performed at the Nuclear Resonance Beamline (BL 11, ID 18) [24] at the European Synchrotron Radiation Facility. The storage ring was operated in the 16-bunch-mode, giving a bunch distance of 176 ns. The monochromatization follows the scheme shown in figure 1, only utilizing different crystal reflections yielding an energy band of $\approx$7 meV (for details cf. [20] and section IV-2.7 in this issue). Spectra below

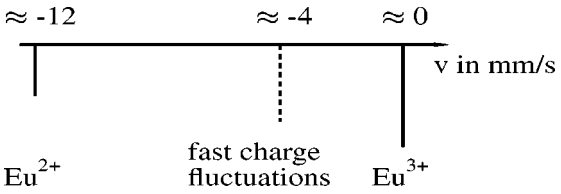

Figure 16. Stick diagram of resonance line positions: low temperatures: two lines, Eu^{2+} and Eu^{3+} coexisting; high temperatures: single line due to fast charge fluctuations.

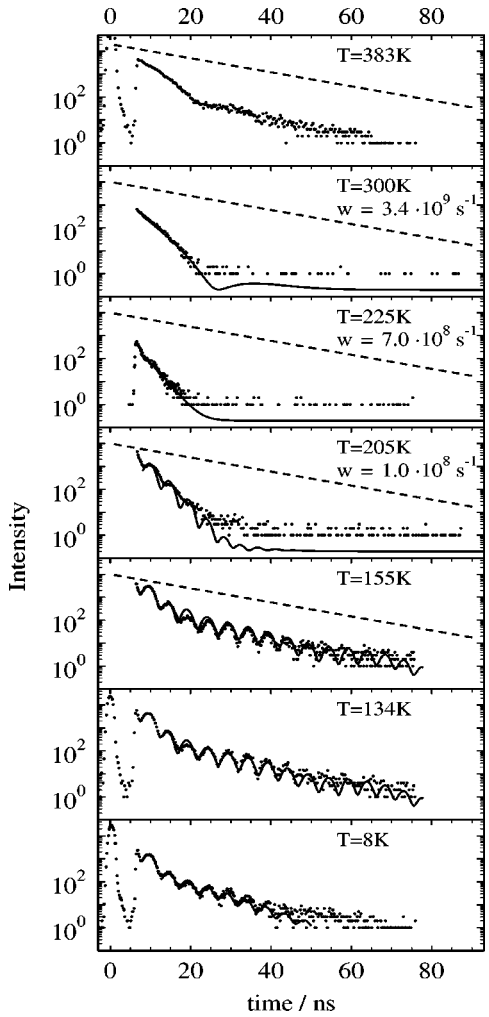

Figure 17. Time spectra of Eu_3S_4 measured at different temperatures. The dashed lines correspond to the decay of a single nucleus (lifetime $\tau = 14.2$ ns). At low temperatures ($T \leqslant 155$ K) spectra are fitted assuming static conditions with two coexisting charge states: Eu^{2+} and Eu^{3+} with a difference in isomer shift of 11.8 mm/s (relative weights 1 : 2). At higher temperatures full lines are simulations assuming fluctuations with frequency w between the two electronic states.

20 K were taken with the sample mounted in a liquid helium bath cryostat. A closed cycle refrigerator established temperatures between ≈20 K and room temperature at the sample, for higher temperatures a furnace was used.

Contrary to standard Mössbauer spectroscopy in the energy domain, where an isomer shift is observed between the radioactive source and the absorber, the Mössbauer spectroscopy in the time domain with a synchrotron radiation source yields the isomer shift with respect to an additional reference scatterer. This technique has been demonstrated in the case of ^{57}Fe [25,26] and enables a precise determination of the isomer shift.

In Eu_3S_4 at low temperatures the Eu^{2+} and Eu^{3+} states coexist in a ratio of 1 : 2, as seen in Mössbauer spectroscopy [22,23]. At temperatures above 200 K charge fluctuations become visible, since the time scale of the fluctuations matches the "hyperfine splitting", here the difference in isomer shift. At 390 K one single sharp line with intermediate isomer shift is observed in the Mössbauer spectra [23]. This is visualized in the stick diagram shown in figure 16.

Therefore, in NFS one expects at low temperatures a pronounced beating even without reference scatterer due to the large difference in isomer shift $\delta_{\mathrm{IS}}(\mathrm{Eu}^{3+}) - \delta_{\mathrm{IS}}(\mathrm{Eu}^{2+}) \approx 12$ mm/s between the two valence states.

NFS experiments on this compound were performed in a temperature range between 4.2 and 390 K. Several spectra are displayed in figure 17. Qualitatively, the expected behavior was observed: the fast beating at temperatures below 155 K and the shift of the nuclear scattered intensity closer to $t = 0$ at higher temperatures. Low temperature data can be fitted by assuming a static coexistence of Eu^{2+} and Eu^{3+} yielding the appropriate relative weights of 1 : 2 and a difference in isomer shift of 11.8 mm/s.

Also the simulations of high temperature spectra, shown in figure 17, qualitatively describe the measured time behavior with the exception of $T = 383$ K. It was assumed in the simulations that the electron configuration statistically flips between the Eu^{2+} and the Eu^{3+} ion shells. The fastest decay is observed at $T = 225$ K. Here the best simulation is achieved when $w \sim 700$ MHz. This fluctuation rate is – within a factor of 3 – comparable to ν_{hf} determined as the difference in isomer shifts of the two charge states.

References

[1] M. Blume, Phys. Rev. 174 (1968) 351.
[2] M.J. Clauser and M. Blume, Phys. Rev. B 3 (1971) 583.
[3] B.V. Thosar and P.K. Iyengar, eds., *Advances in Mössbauer Spectroscopy* (Elsevier, Amsterdam, 1983).
[4] O. Leupold, E. Gerdau, H.D. Rüter, W. Meyer-Klaucke, A.X. Trautwein and H. Winkler, HASYLAB Annual Report I (1996) 73.
[5] A.Q.R. Baron, Nucl. Instrum. Methods A 352 (1995) 665.
[6] H. Winkler, E. Bill, A.X. Trautwein, A. Kostikas, A. Simopoulos and A. Terzis, J. Chem. Phys. 89 (1988) 732.

[7] R.A. Edmonds, *Angular Momentum in Quantum Mechanics* (Princeton Univ. Press, Princeton, 1957).
[8] M. Haas, E. Realo, H. Winkler, W. Meyer-Klaucke, A.X. Trautwein, O. Leupold and H.D. Rüter, Phys. Rev. B 56 (1997) 14082.
[9] E.L. Bominaar, X.-Q. Ding, A. Gismelseed, E. Bill, H. Winkler, A.X. Trautwein, H. Nasri, J. Fischer and R. Weiss, Inorg. Chem. 31 (1992) 1845.
[10] W. Sturhahn and E. Gerdau, Phys. Rev. B 49 (1994) 9285.
[11] S.C. Bhargava, J.E. Knudsen and S. Mørup, J. Phys. C 12 (1979) 2879.
[12] O. Leupold, A. Bernhard, E. Gerdau, J. Jäschke, H.D. Rüter, Y. Shvyd'ko, H. de Waard, E.E. Alp, P. Hession, M. Hu, W. Sturhahn, J. Sutter, T. Toellner, A.I. Chumakov, J. Metge and R. Rüffer, Hyp. Interact. 113 (1998) 81.
[13] WWW site `http://www.aps.anl.gov/sricat/3id.html`.
[14] T.S. Toellner, E.E. Alp, W. Sturhahn, T.M. Mooney, X. Zhang, M. Ando, Y. Yoda and S. Kikuta, Appl. Phys. Lett. 67 (1995) 1993.
[15] M. Blume and R. Orbach, Phys. Rev. 127 (1962) 1587.
[16] S. Mørup, J.A. Dumesic and H. Topsøe, in: *Applications of Mössbauer Spectroscopy*, Vol. 2, ed. R.L. Cohen (Academic Press, New York, 1980) p. 1.
[17] H. Winkler, W. Meyer, A.X. Trautwein and B.F. Matzanke, Hyp. Interact. 91 (1994) 841.
[18] H.H. Wickman, in: *Mössbauer Effect Methodology*, Vol. 2, ed. I.J. Gruverman (Academic Press, New York, 1966) p. 39.
[19] M. Haas, E. Realo, H. Winkler, W. Meyer-Klaucke, A.X. Trautwein and O. Leupold, to be published in Phys. Rev. (1998).
[20] O. Leupold, J. Pollmann, E. Gerdau, H.D. Rüter, G. Faigel, M. Tegze, G. Bortel, R. Rüffer, A.I. Chumakov and A.Q.R. Baron, Europhys. Lett. 35 (1996) 671.
[21] C.M.P. Barton and N.N. Greenwood, in: *Mössbauer Effect Data Index*, eds. J.G. Stevens and V.E. Stevens (Plenum, New York, 1973) p. 395;
F. Grandjean and G.J. Long, in: *Mössbauer Spectroscopy Applied to Inorganic Chemistry*, Vol. 3, eds. G.J. Long and F. Grandjean (Plenum, New York, 1989) p. 513.
[22] O. Berkooz, M. Malamud and S. Shtrikman, Solid. State Commun. 6 (1968) 185.
[23] B.C. Bunker, R.S. Drago and M.K. Kroeger, J. Amer. Chem. Soc. 104 (1982) 4593.
[24] R. Rüffer and A.I. Chumakov, Hyp. Interact. 97/98 (1996) 589.
[25] E.E. Alp, W. Sturhahn and T. Toellner, Nucl. Instrum. Methods B 97 (1995) 526.
[26] O. Leupold, H. Grünsteudel, W. Meyer, H.F. Grünsteudel, H. Winkler, D. Mandon, H.D. Rüter, J. Metge, E. Realo, E. Gerdau, A.X. Trautwein and R. Weiss, in: *Proc. of Conf. ICAME-95*, Vol. 50, ed. I. Ortalli (SIF, Bologna, 1996) p. 857.